Full Length Article

Magnetically navigable 3D printed multifunctional microdevices for environmental applications

Roberto Bernasconi[a,*], Elena Carrara[a], Marcus Hoop[b], Fajer Mushtaq[b], Xiangzhong Chen[b], Bradley J. Nelson[b], Salvador Pané[b], Caterina Credi[c], Marinella Levi[c], Luca Magagnin[a]

[a] Dipartimento di Chimica, Materiali e Ingegneria Chimica Giulio Natta, Politecnico di Milano, Via Mancinelli 7, 20131, Milano, Italy
[b] Multi-Scale Robotics Lab, Institute of Robotics and Intelligent Systems, ETH Zurich, Tannenstrasse 3, 8092, Zurich, Switzerland
[c] Dipartimento di Chimica, Materiali e Ingegneria Chimica Giulio Natta, Politecnico di Milano, Piazza Leonardo da Vinci 32, 20133, Milano, Italy

ABSTRACT

Microrobotic prototypes for water cleaning are produced combining stereolithography 3D printing and wet metallization. Different metallic layers are deposited on 3D printed parts using both electroless and electrolytic deposition to impart required functionalities. In particular, by exploiting the flexibility and versatility of electrolytic codeposition, pollutants photodegradation and bacteria killing are for the first time combined on the same device by coating it with a composite nanocoating containing titania nanoparticles in a silver matrix. The microstructure of the microrobots thus obtained is fully characterized and they are successfully actuated by applying rotating magnetic fields. From the water cleaning point of view, devices show evident photocatalytic activity towards water pollutants and antimicrobial activity for gram negative bacteria.

1. Introduction

Chemogenic and biogenic water contamination is among the main problems for public healthcare worldwide, and especially in developing countries. Low quality sewer networks or uncontrolled spills of toxic industrial wastes are factors that strongly influence the quality of life for billions people all over the world. Approximately, the total amount of wastewater produced annually by human activities is about 1500 km^3 (equivalent to six times more the amount of water contained in all the rivers of the world) [1]. Polluted water is a source of a great number of diseases caused by pathogens, such as cholera or dysentery, or by chemical agents, like chronic poisoning or cancer [2]. Therefore, effective water remediation strategies must synergistically target both the detoxification of harmful bacteria, viruses or protozoa as well as the removal of toxic chemicals. Many approaches used for water quality improvement are based on the addition of chlorine containing species (chlorination) to eliminate dangerous pathogens [3], or on techniques such as chemical coagulation or chemisorption on active materials to remove chemicals [4]. However, some chemicals are considerably difficult to eliminate using conventional techniques. For example, azo dyes cannot be efficiently oxidized or aerobically digested [5–7]. Current state-of-the-art methods are in many cases costly, or far from being environmentally friendly. In this regard, last few decades have seen a growing demand for low cost and green alternatives to common water remediation methods.

Untethered small-scale machines [8–11] have been recently proposed as potential mobile environmental micro- and nanocleaners. The ability of these micro- and nanodevices for swimming [12,13] provides several advantages over other micro- and nanoparticulates for water cleaning applications. First, micro- and nanomachines could act in difficult-to-access locations such as pipes or conductions. Furthermore, the reactions involved in the degradation of products can be enhanced as these small-scale cleaners could distribute washing chemical agents, or act as mobile catalysts, mixers or adsorbing platforms. A drawback of these swimmers is that many of them cannot be recovered. Several types of micro- and nanomachines, in terms of their locomotion features, have been reported for their use as water-remediation small-scale agents. For example, several groups have shown different pollutant treatments exploiting catalytically propelled motors [14–16]. In contrast, other groups have designed different types of magnetically driven micro- and nanoplatforms for water cleaning applications, including organics degradation [17] or bacteria killing [18]. Apart from their recoverability, these devices exhibit a wide variety of locomotion patterns and can be programmed [19] to scan regions of water waste containers or lines.

Here, we present a magnetically controlled 3D printed cylindrical

microrobotic prototype, which is able to target simultaneously the degradation of organic pollutants and the killing of bacteria. Such prototype is characterized by dimensions ranging between hundreds of micrometers to millimeters, similarly to other microrobots described in literature [20–22]. The device is fabricated by means of 3D printing [23] and wet metallization [24–26], which are both low-cost manufacturing processes. Additionally, these fabrication techniques can be easily operated, and allow for a batch production of parts or devices [22]. Both 3D printing and wet metallization, however, present considerable challenges when applied to microfabrication. Stereolithography (SLA) at the microscale [27] is widely employed to manufacture functional devices [28–31], but manufacturing possibilities are in many cases limited by resolution and by the need to use printing supports. Even the use of wet metallization introduces some challenges that must be addressed, including for example the necessity to handle the devices in the plating solutions. In addition, wet metallization techniques are characterized by some intrinsic peculiarities. For instance, while electroless deposition is highly conformal from the layer thickness point of view [32], electrolytic deposition is influenced by electric field distribution inhomogeneity. This implies that, for complex shapes, it is hard to obtain a constant thickness on the device. Electrolytic deposition is however advantageous in terms of plating speed and variety of materials if compared to electroless plating. When correctly implemented, however, stereolithography and wet metallization allow to combine the impressive flexibility of polymer based 3D printing with the possibility to apply new functionalities introduced by metallization.

Stereolithographically printed microdevices were produced and first metallized with a magnetic layer to enable remote navigation under the action of a magnetic field, and subsequently coated with an active composite consisting of a silver matrix with embedded titania nanoparticles. The magnetic layer was made of a hard-magnetic alloy [33], which allowed for programming its magnetization axis. Silver was selected as it is one of the most effective antibiotic materials [34–37]. The biocidal activity of silver is based on its ability to induce denaturation of bacterial membrane proteins, to inhibit some vital enzymes and to interact with proton exchange mechanisms. Silver is especially effective against highly drug resistant gram-negative bacteria [38] and presents minor toxicity towards superior organisms [39]. Titania (TiO_2) was primarily chosen for its high photocatalytic activity [40], which can be further optimized doping the material [41–43]. In fact, one of the most promising techniques for organic pollutants elimination is the advanced oxidation process (AOP), which is based on the oxidation of organic compounds by reactive radicals generated on the surface of semiconductor photocatalysts [44,45]. The biocidal activity of silver and the photocatalytic properties of titania can be combined in a composite material to achieve integrated water cleaning functionalities, as demonstrated in recent literature [46,47] in the case of chemical vapor deposited layers. In order to combine silver and titania in the same platform, however, electrochemical codeposition is the most attractive method as it allows the easy and cost effective growth of dispersion coatings made of metallic matrices with embedded ceramic micro- or nanoparticles [48–51]. Additionally, this method can be used to uniformly coat intricate structures such as those 3D printed in this work using a subset of the plating technology called barrel plating. A main issue in the case of electrolytic deposition on millimeter-sized objects is the electrical contact with the generator to close the anode/cathode cell. Here, we capitalize on a technique typically employed in the industry for small parts that require galvanic treatments called barrel plating. In barrel plating, a large number of objects is placed inside a container able to conduct electricity [52]. The contact between the parts and the container and between the parts themselves makes possible the passage of electrons and the subsequent electroreduction of the desired metallic ions at the surface. The container is typically put in rotation to allow uniform deposition.

2. Experimental methods

A urethane-acrylate based resin (DL260 by DWS) filled with 20% m/m silica-alumina powder was employed for SLA printing of the devices. A commercial stereolithography machine, model 028 J Plus produced by Digital Wax Systems (DWS), was used. Such machine mounted a monochromatic laser Solid State Bluedge BE-1500 A/BE-1500AHR with galvanometer control, characterized by an emitting power of 30 mW, a wavelength of 405 nm, a beam spot diameter of 22 μm and a vertical (z-axis) resolution of 10 μm. CAD models were designed using Solidworks software (Dassault Systèmes, France) and cylindrical microdevices (whose design is visible in Figs. S1 and S2) were printed in two shapes, namely PL (planar) and SP (spiral). Table S1 reports nominal dimensions for PL and SP samples. Prior to the printing step, the 3D virtual models were processed with a specific 3D parametric software (Nauta +, DWS systems), and reoriented on the working platform to ensure the highest printing resolution. Printing supports were introduced by exploiting a dedicated command (Autosupport), enabling to introduce cylindrical pillars with a height of 2 mm and diameter ranging between 200 μm and 500 μm. The resulting processed virtual models were subsequently sent to Fictor (DWS Systems), the software machine that directly controls the 3D printer, and numerically sliced according to the user-imposed building parameters. Laser speed ranged between 250 and 4300 mm/s and the layer thickness between 25 and 10 μm. After the SLA printing step, the samples were washed in ethanol to remove unreacted resin, dried with nitrogen, and then post-cured by further exposition to UV radiation for 30 min (λ = 405 nm, Model S Ultraviolet Curing Unit, DWS). The UV post-curing step is meant to crosslink any uncured liquid resin within laser-scanned adjacent lines and to accomplish the total polymer conversion.

Samples were removed from the printing supports and subjected to an electroless metallization treatment. All the chemicals employed for the metallization process were purchased from Sigma Aldrich and used as received. The devices were cleaned for 4 min at T_a in a solution containing Na_2CO_3 (50 g l^{-1}), Na_2SiO_3 (35 g l^{-1}), $C_{12}H_{25}NaSO_4$ (3 g l^{-1}). No stirring was used and the devices were immersed in the solution and subsequently filtered out at the end of the cleaning step. After washing with deionized water, the surface of the samples was etched for 30 min in a KOH solution (200 g l^{-1}) at 45 °C. Also in this case no stirring was used and the samples were recovered by filtering them out of the solution. The surface was carefully washed with water to avoid contamination of the subsequent solutions. Surface was activated for electroless deposition using a Sn-free activation process comprising two steps: immersion for 5 min in a Pd based commercial activator (Neoganth 834 by Atotech) and subsequent immersion for 30 s in a reducing bath composed of $NaBH_4$ (20 g l^{-1}). No stirring was employed and activation was performed three times on the devices. The devices were not washed after the immersion in the Neoganth activator but they were rinsed after the passage in the reducing solution. A first copper layer was deposited using an alkaline electroless bath containing the following components: $CuSO_4$·$5H_2O$ (20 g l^{-1}), Na_2EDTA (40 g l^{-1}), $C_{10}H_8N_2$ (10 mg l^{-1}), $Fe(CN)_6$ (10 mg l^{-1}), $C_2H_2O_4$ (10.5 g l^{-1}) [53]. Deposition was performed at 45 °C and pH 12 for 15 min. The microdevices were free to move in the solution thanks to the vigorous agitation that left them in suspension. At the end of the electroless metallization, they were recovered from the solution by filtering, washed in deionized water and dried with nitrogen. CoNiP, Cu and Ag/TiO_2 were applied placing the samples in a metallic basket realized employing a stainless steel net characterized by 250 μm as wires diameter and pore size of 800 μm. Dimensions of the basket were 2 cm × 0.7 cm and 10 samples were placed in it. Samples were washed with deionized water after each metallization step. CoNiP electrolytic bath formulation was based on the following components: $NiCl_2$·$6H_2O$ (25.92 g l^{-1}), $CoCl_2$·$6H_2O$ (26.74 g l^{-1}), NaH_2PO_2·H_2O (12.84 g l^{-1}), NaCl (40.91 g l^{-1}), H_3BO_3 (24.72 g l^{-1}), saccharine (0.88 g l^{-1}) [33]. pH was set to 3,

no stirring was employed and deposition was performed at room temperature and 10 mA cm^{-2}. Copper was deposited from a commercial acidic solution, Hard Copper CU-200 (by Reprochem), at ambient temperature, moderate stirring and 10 mA cm^{-2}. Silver/titania codeposition was performed employing a commercial silver plating solution Silveron GT-101 (by Dow Electronic Materials), additivated with Degussa P-25 titania nanoparticles (20 g l^{-1}). Deposition was performed at pH 9.5, 45 °C, 30 mA cm^{-2} and vigorous stirring to keep in suspension titania particles. Deposition times were selected as detailed in the results and discussion part to achieve a 5 μm thick layer for CoNiP and a 6 μm thick for Ag/TiO$_2$. Fig. S3 describes the complete metallization process, including both electroless and electrolytic metallization.

For SEM characterization, a Zeiss EVO 50 microscope was employed. The instrument was equipped with an Oxford Instruments Model 7060 EDS module, which was used to study composition of deposited films. A Leica DMLM direct illumination microscope was used to analyze the section of the samples. The atomic force microscope used in this work is a NT-MDT SOLVER PRO. Magnetic properties of the materials were evaluated by mean of a Princeton Measurement Corp. MicroMag 3900 vibrating sample magnetometer (VSM) system. Magnetic actuation was performed employing the Octomag manipulation system [54]. Samples behavior was evaluated using air, water and AP 100 siliconic oil (Sigma Aldrich) as medium.

Photodegradation tests inspired to the ISO standard were performed [55]. A 2 mg l^{-1} rhodamine B (Rh B) solution was employed and the samples were illuminated using a UV lamp Spectroling EN-160 L/FE having nominal power 6 W and emitting at 365 nm. Intensity on the samples was found to be 2.23 mW cm^{-2}. 3 samples were placed 4.5 cm far from the lamp in 1 ml of Rh B solution. Absorbance was measured by mean of a UV–vis spectrophotometer Tecan Infinite 200 Pro.

Microrobots biokilling was quantified by counting colony-forming units (CFU). Clinically isolated methicillin resistant *Staphylococcus aureus* ZH124 (University Zurich, Zurich, Switzerland) was grown in Brain Heart Infusion (BHI) media overnight prior to antimicrobial tests. Bacterial density has been determined by OD600 measurements and adjusted to 0.5. Microrobots were cleaned with a 70% ethanol solution and incubated overnight with bacterial cells at 37 °C. The magnetic structures were then removed and 100 μL of the bacterial suspension was distributed on a BHI agar plate at different dilutions (10^{-1}, 10^{-2}, 10^{-3}, 10^{-4}, 10^{-5}, 10^{-6}, 10^{-7}). Only 10^{-3}, 10^{-5} and 10^{-7} dilutions were analyzed. The plates were further incubated at 37 °C for 24 h and bacteria viability was determined by counting the colony forming units.

The cells used for biocompatibility tests were mouse 3T3 fibroblast (atcc) cultivated using standard methods, in 24-well flat bottomed tissue culture plates of good optical quality. The final volume of tissue culture medium in each well should be 0.1 mL, and the medium (DMEM) may contain up to 10% Fetal Bovine Serum to be at physiological conditions. The MTT Cytotoxicity study was conducted in well plates with 1×10^4 3T3 cells in culture medium (100 μL). They were incubated at 37 °C for cleavage of MTT to occur. Optimal times may vary according to the assay, but four hours were found to be suitable for the purposes of this work. At the end of this time, the MTT formazan produced in wells containing live cells appeared as black, fuzzy crystals on the bottom of the well. Cell medium was removed, and then cells were washed with PBS and exposed to microrobots. After 2 days of incubation, the supernatant was replaced by fresh media (100 μL) and supplemented with CTO2 MTT. After 4 h of incubation, isopropanol (100 μL) and HCl (0.04 M) were added to each well and they were mixed thoroughly by repeated pipetting. Finally, absorbance measurements were conducted in a microtiter plate reader (Tecan Infinite 200 Pro) at 540 nm and a reference wavelength of 630 nm.

3. Results and discussion

3.1. Devices manufacturing and characterization

The devices manufactured in the present work were 3D printed using stereolithography. This technique is suitable for the costless realization of millimetric sized microrobots presenting complex shapes. As a matter of fact, millimetric devices were successfully printed within 30 min, thus highlighting the huge impact that 3D printing processes have on decreasing the overall time of the microfabrication process respect to time consuming standard lithographic-based technologies. Moreover, printed microdevices were characterized by excellent physical integrity as well as a well-defined and reproducible architecture. SEM and optical microscopy were employed to measure experimental features in printed parts, which were compared with theoretical ones. Deviations of more than 20 μm from the nominal dimensions were never observed. Dimensions in the millimeter range were considered because the target application, unlike most of the current literature on microrobotics, is outside human body. The shape of the microdevices was studied to improve their functional properties. Keeping in mind the need of a cylindrical outer surface for rolling motion, the specific area was increased by creating a series of protrusions (according to the scheme showed in Figs. S1 and S2). Such protrusions were printed separated one from the other (Fig. S1) to form plates or linked together to form a spiral on the device (Fig. S2). Consequently, two different geometries, namely PL (plates) and SP (spiral) were tested. The usage of these two morphologies allowed the investigation of the effect of microdevice shape on the speed and actuability of the devices. In fact, the fluidodynamic properties of the two device versions are different, resulting in different behaviors according to the type of fluid in which they are immersed. Fig. 1b depicts how a PL sample looks like after the printing step. Fig. S6 describes the morphology of the 3D printed DL260 surface on a PL sample. Weight of as printed devices was found to be 15.5 ± 0.4 mg for PL samples and 18.2 ± 0.3 mg for SP samples.

After being printed, the devices were coated with functional layers to provide magnetic actuation and photocatalytic/antimicrobial activity. Fig. 1a describes the internal structure of the devices and the sequence of the metallic layers applied on the surface of the 3D printed resin. A first layer of pure copper was applied to the surface of the devices by electroless deposition. The function of this first layer is to provide electrical conductivity to the surface for subsequent electrolytic deposition of the magnetic CoNiP layer. Fig. S3 shows a scheme of the deposition process. The electroless step has already been described elsewhere in detail [24]. Roughly, 400 nm of electroless copper were deposited by immersing the devices in the electroless plating solution and the resulting layer was found to be adherent and conductive enough to allow electrodeposition of further layers. Fig. 2a shows the morphology of the layer observed with SEM, while Fig. 1c depicts the appearance of the samples after the first Cu layer.

The devices described in the present work were placed inside a stainless steel basket (visible in Fig. 1c, d and e). Such container was connected to a generator to provide current and immersed in an electrolytic bath, as shown in Fig. S4. Periodically, the basket was shaken to remove hydrogen bubbles and to change the contact zone of the samples to allow uniform deposition. The last step of the devices fabrication comprised the electrolytic deposition of the different functional alloys (Fig. S3). Barrel plating presents significant advantages with respect to electroless deposition: a larger selection of materials can be plated, at high plating rates and with less electrolyte management issues. The main disadvantage with respect to electroless is the unequal thickness of the plated layers on complex geometries, which is the result of inhomogeneities in electric field distribution. Other techniques can be used to provide electrical contact on small parts, but barrel allows uniform deposition without leaving unplated regions. A direct contact established on the surface of the parts would leave, for instance, small zones deprived of plated metal. The application of barrel plating
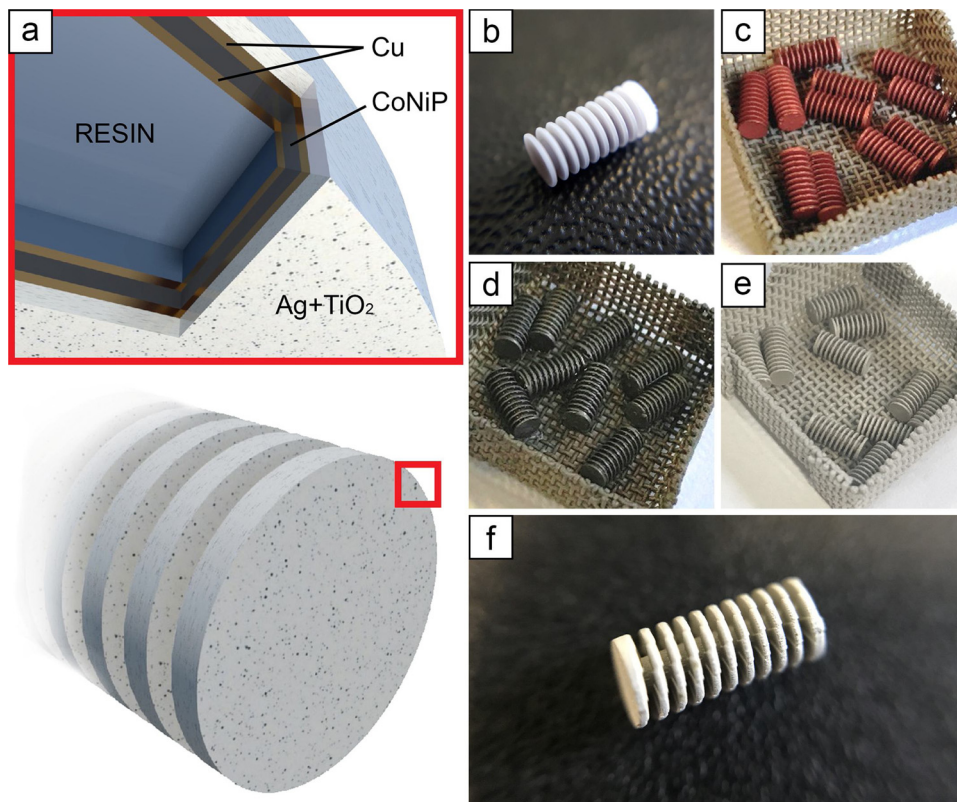
Fig. 1. Internal structure of the photoactive/antimicrobial devices (a); device appearance after 3D printing (b); devices placed in the barrel setup after electroless Cu deposition (c); devices after CoNiP deposition (d); devices after Ag/TiO$_2$ plating (e); final microrobots appearance (f).
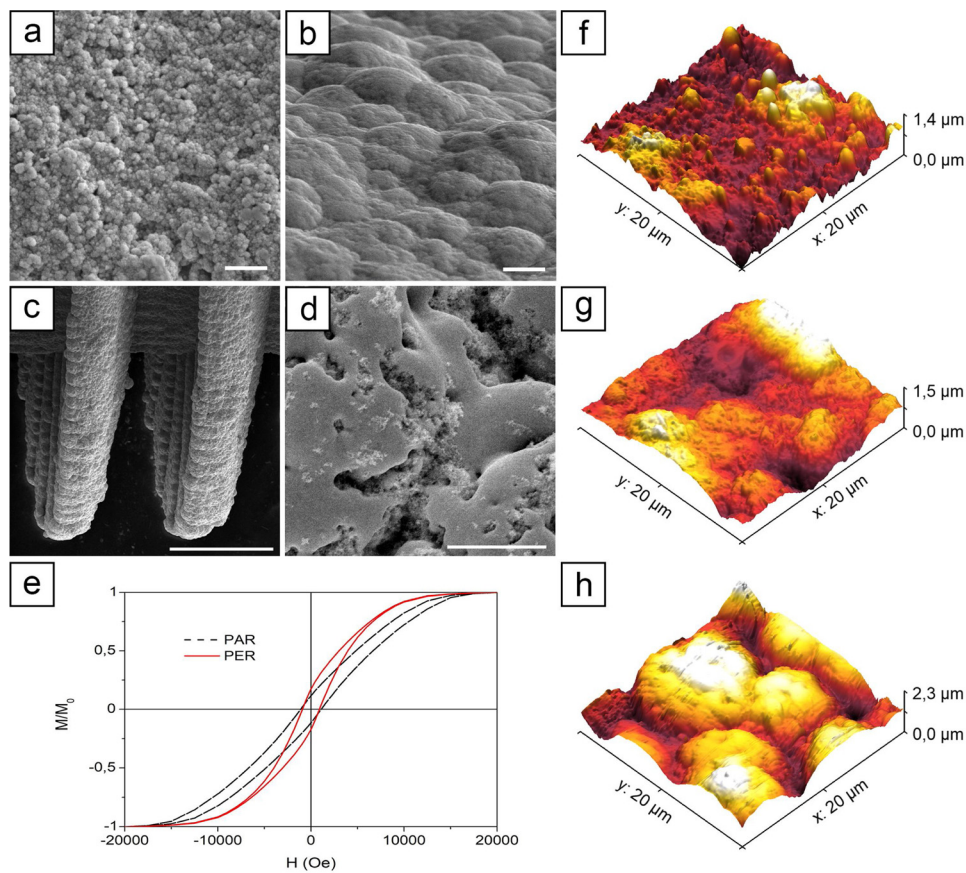

Fig. 2. Morphology of the initial electroless Cu layer employed to impart conductivity to the 3D printed surface (a), scale bar is 2 μm; morphology of the CoNiP layer (b), scale bar is 2 μm; structure of a metallized SP sample (c), scale bar is 400 μm; surface morphology of the final Ag/TiO$_2$ composite (d), scale bar is 4 μm; VSM characterization of a PL sample coated with CoNiP (e); AFM characterization of an uncoated (f), Cu/CoNiP coated (g) and Cu/CoNiP/Cu/Ag/TiO$_2$ coated (h) device.

requires, however, a careful control on metallization process, as this technique is characterized by growing rates that are not linearly dependent on the quantity of electrical charge provided to the surface of the piece. Faraday law for electrolysis (Eq. 1) states that the quantity of ions reduced is a function of their valence, their molar mass and of the total quantity of electrons employed.

$$m = \frac{Mq}{ZF} \tag{1}$$

m is the total mass reduced, M is the molar mass of the metal being deposited, q is the total electric charge used, Z is the valence of the ions reduced and F is the Faraday constant. If cathodic efficiency is 100%, all the charge is used to reduce the metal, otherwise parasitic hydrogen evolution reactions are present. In the case of barrel plating, electrical contact is not ideal (unlike in the case of rack plating) and for this reason apparent deposition efficiency is lower. The reason for such non-ideal electric conduction is the small contact area between the samples and the basket, and between the samples themselves. Apparent deposition efficiency varies as a function of the shape of the objects, the number of objects inside the basket and the current employed. Eq. 2 describes the amount of metal deposited if cathodic efficiency (η) and apparent barrel efficiency (ψ) are considered.

$$m = \frac{Mq}{ZF} \eta \psi \tag{2}$$

By considering Eq. 2, it is obvious that the current provided to the basket must be increased with respect to the nominal one prescribed for rack plating to achieve the same growth rate (amount of deposited metal m). An alternative approach to achieve a similar thickness than in electrodeposition on planar substrates consists of increasing deposition time. To calculate the value of ψ for the barrel system considered, different alloys were deposited on a planar substrate and the resulting grow rate was compared with that obtained from barrel plating. A thickness value measured on the flat round face of the device was considered to avoid effect of geometry on current distribution. Such value of apparent efficiency must be in general recalculated when plating conditions are changed. In addition, the number of samples present in the barrel plays a role on the efficiency of the metallization. In particular, a load of 10 samples for each metallization batch was considered. Table 1 reports the parameters calculated for CoNiP and Ag/TiO$_2$ plating.

The first functional layer deposited on the electroless copper was a CoNiP coating. CoNiP is a semi-hard magnetic alloy that can be premagnetized to allow rolling actuation of the devices. 5 μm of such material were deposited on the copper by barrel deposition. To achieve the desired thickness, deposition time was increased 4 times with respect to a planar sample. Current was not modified, as the variation of this parameter was found to alter the composition of the alloy, which is optimized to achieve the maximum magnetic hardness [33]. Composition was determined by EDS: 3.08% wt. P, 84.75% wt. Co and 12.24% wt. Ni. Fig. 2b depicts the appearance of the CoNiP coating when observed via SEM. The typical nodular surface of an electrodeposited layer is visible. Fig. 1d depicts the visual appearance of the samples after CoNiP application.

One of the main disadvantages of using electrolytic deposition is the unequal thickness distribution of the layer in different regions of the device. Fig. S5 shows the thickness variation of the CoNiP coating in some significant places of the microdevice. In particular, the CoNiP

Table 1
Barrell plating parameters to achieve a 5 μm thick deposit in the case of CoNiP and a 6 μm thick in the case of Ag/TiO$_2$ and comparison with planar samples.

	Plating time (planar sample)	Plating time (barrel)	η	ψ
CoNiP	40 min	160 min	0.42	0.25
Ag/TiO$_2$	15 min	45 min	~1	0.33

thickness was evaluated on the edge of the blades, and at the bottom of the space between the blades. These two regions, being characterized by diametral opposite conformations, were expected to experience significantly different electric field densities (resulting thus in different final CoNiP thicknesses). A parameter called conformability, defined as the ratio between the lowest (space between the blades) and highest (edge of the blades) value of thickness recorded in the different parts of the layer, can be calculated. Such parameter is indicative of plating uniformity and it is close to 100% when the thickness is the same on the entire sample. Electroless plating in most cases presents conformabilities close to 100%, as a chemical reaction is exploited to perform deposition. Conversely, when an electric field is present, its distribution is a function of the geometry of the piece. In some regions, this results in decreased deposition rates. Conformability is not only a function of geometry but also of the electrochemical reaction taking place, e.g. of the alloy deposited. In the case of CoNiP deposition conformability was found to be 86%, which was sufficient for the magnetic actuation of the device. In fact, the main variable that determines the force applied on the device is the quantity of magnetic material and not its distribution.

To evaluate actuality of the devices, magnetic properties of the CoNiP layer were investigated using VSM. Fig. 2e depicts the result obtained, where a clear semi-hard magnetic behavior can be observed. The PAR direction refers to an orientation of the magnetic field parallel to the axis of the device, while the PER direction refers to an orientation of the magnetic field perpendicular to the axis. Values of coercivity varied between 1107 Oe (PAR) and 915 Oe (PER). The two hysteresis cycles observed are similar as a consequence of the shape of the device. Being the sample cylindrical and full of surfaces variously oriented, the grow direction of the CoNiP presents many possible orientations. For this reason, magnetic anisotropy of the CoNiP layer [33] is compensated by the presence of many CoNiP grow directions.

A thin copper flash was deposited as third layer between the CoNiP layer and the silver composite. The only function of such coating is to provide adhesion to the subsequent silver/titania layer. It was observed that delamination occurs if the composite is directly plated on top of the magnetic layer, as a consequence of possible passivation of CoNiP in the slightly alkaline silver bath. Conversely, an adherent copper coating can be easily obtained by depositing copper from a commercial acidic sulfate electrolyte. 400 nm of copper were therefore deposited on the devices. Electroless deposition was not employed for deposition of the flash layer, since the surface of the samples was conductive due to the presence of the initial electroless Cu layer and the subsequent CoNiP coating. Consequently, electrolytic Cu deposition was performed. This technique presents higher grow rates with respect to electroless deposition and a better surface finishing.

The fourth and final layer applied on the devices was the silver/titania composite (Fig. 1e). Its SEM appearance is depicted in picture 2d, where titania particles are clearly visible inside the silver matrix. Large nodules are visible in the figure, together with pores probably connected to the presence of titania particle. The amount of codeposited titania was evaluated by mean of EDS and it was found to be 4.7% wt. Conformity in this case was found to be 80%. In the case of Ag/TiO$_2$ deposition, current was increased 3 times to 30 mA cm^{-2} to compensate the barrel and time was kept constant with respect to the planar sample. It was observed that the codeposition of titania was determined by the real current density on the sample more than the plating time. By increasing plating time instead of current, very low titania codeposition was observed. Total current was therefore multiplied to compensate the measured ψ. Final weight of the devices after metallization was found to be 34.6 ± 0.7 mg for PL devices and 36.7 ± 0.2 mg for SP devices.

Final SEM appearance of the samples is visible in Fig. S7 (PL) and S8 (SP). In Fig. 2c, the stepped shape of the blades in the case of a SP sample can be observed. Such stepped surface is a result of the layer-by-layer building of the structure during SLA 3D printing. It can be
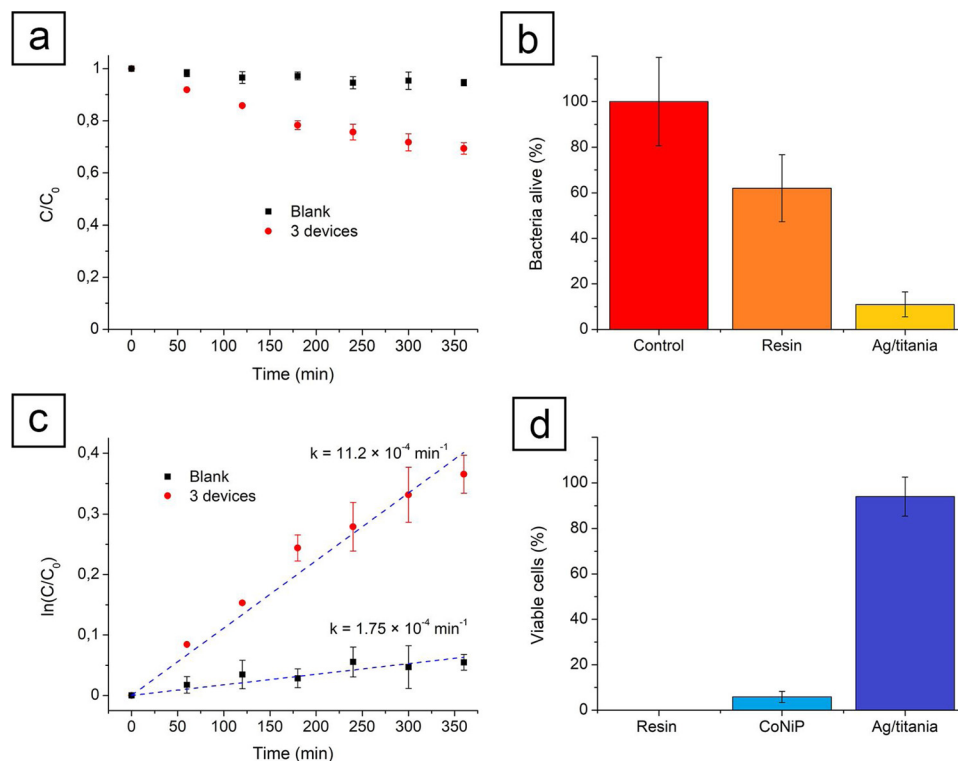
Fig. 3. Photocatalytic behavior of the devices towards Rh B (a and c); biocidal activity of the devices towards gram negative *Staphilococcus Aureus* bacteria(b); microrobots biocompatibility for mouse fibroblasts (d).

observed that the metallic layer uniformly covers the surface of the samples. Surface roughness and morphology were evaluated employing AFM and laser profilometry. Analysis was limited to a $20 \times 20\,\mu m$ to limit the influence of roughness induced by the presence of printing steps. As visible in Fig. 2f–h, surface roughness progressively increases when new layers are added to the surface. This was expected, since non-additivated electroplating solutions normally amplify initial substrate roughness. Consequently, initial roughness plays a fundamental role in determining final morphology. Values of R_a varies from 196 nm in the case of the uncoated resin (Fig. 2f) to 265 nm for the CoNiP coated (Fig. 2g) and 378 nm for the composite layer (Fig. 2h). The nodular structure of the layer is visible also with AFM.

3.2. Photocatalytic activity

Devices functionality was verified performing separated tests for photodegradation and antibacterial behavior. Fig. 3a and c depict the photocatalytic activity of 3 devices placed in a Rh B solution with respect to a reference solution without any microrobot. Fig. 3a reports the data as ratio between the initial concentration C_0 and the concentration C at time t. Fig. 3c, on the contrary, reports the same data represented using the logarithm of such ratio. Degradation of Rh B upon exposition to UV light follows a linear trend in the logarithmic representation, as confirmed previously [56,57]. This is indicative of a first order reaction having a constant k around $1.75 \times 10^{-4}\,min^{-1}$, as extrapolated by the linear fitting of the data according to Eq. 3.

$$ln\left(\frac{C}{C_0}\right) = -kt \tag{3}$$

The behavior visible in Fig. 3c, with the devices presenting a photodegradation path less linear than the blank solution, can be mainly attributed to their cylindrical shape, which means unequal distribution of light intensity on the surface (with some parts of the sample illuminated at considerably low angles). It is well known that an inhomogeneous distribution of light intensity can lead to apparent

reaction orders higher than one [58]. Another possible factor influencing linearity is the possibility of back reflections coming from the bottom of the container. Such reflections hit the part of the devices that is not directly illuminated by the UV lamp, resulting in uncontrolled photocatalytic reaction of unknown order. If a first order approximation is considered in the case of the devices, linear fitting of the data presented in Fig. 3c according to Eq. 3 leads to a value for k of $11.2 \times 10^{-4}\,min^{-1}$. Such value is more than six times with respect to the one measured without devices. Degradation speed of Rh B is therefore considerably increased by the presence of the silver/titania coated microrobots. Measured k is a function of the number of devices, e.g. the area of active material exposed to UV light.

3.3. Antimicrobial activity

The antimicrobial activity of individual devices was assessed in terms of percentage of bacteria left. In Fig. 3b, one can see that uncoated 3D printed specimens were able to perform a limited biokilling action with a 62% of bacteria still alive. The killing ability is probably a consequence of unreacted residues from the resin that are released in the environment. This observation is also supported by the fact that uncoated 3D printed structures exhibit a low biocompatibility (Fig. 3d). In contrast, silver/titania coated samples display a substantial bacteria killing activity, with a 11% of the bacteria alive. This data demonstrates a significant antibacterial activity of a single device. Note that antibacterial effect is a function of the number of the devices used with respect to the quantity of contaminated water and of the exposure time. These two factors can be actively tuned to enhance the number of bacteria killed. Total water disinfection (no bacteria left alive) is typically not possible, as demonstrated also by other approaches presented in the literature [18].

Another advantage of silver with respect to other antibiotic agents is its relatively low cytotoxicity towards mammalian cells [59]. Cytotoxicity of the devices was evaluated using fibroblasts. As anticipated before, SLA resin is not biocompatible, resulting in a 0% cell viability.
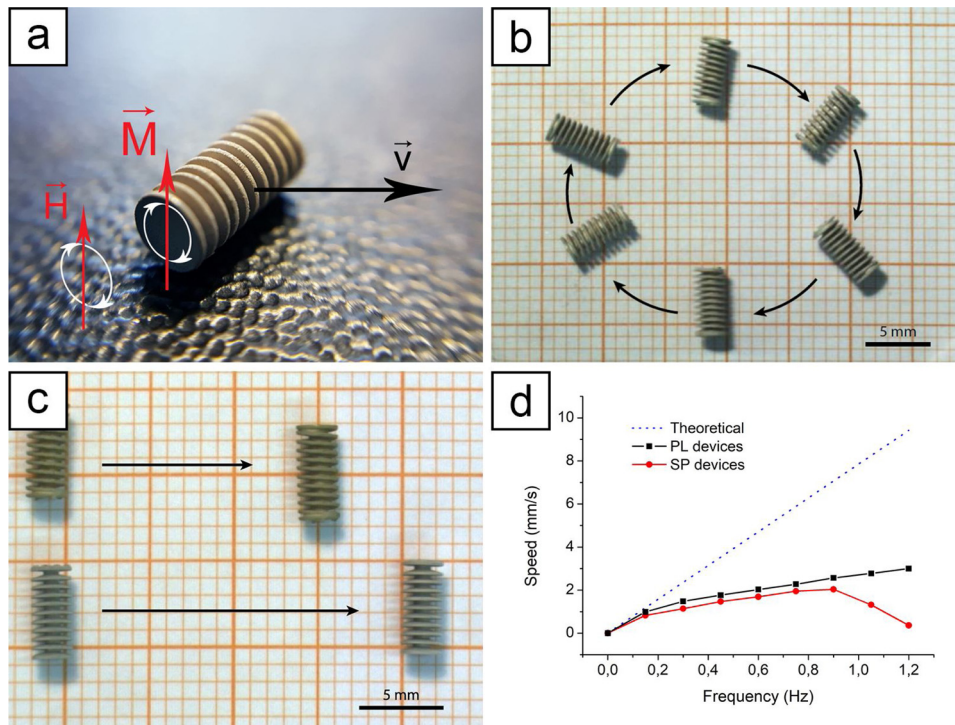
Fig. 4. Rolling actuation principle (a); Rolling actuation along a circular pattern (b); simultaneous actuation of two samples, SP and PL, in silicone oil (c); speed vs. external field rotation frequency relationship for SP and PL samples in silicone oil (d).

CoNiP alloy is not biocompatible as well, with cell viability in the order of 5.8%, while the Ag/TiO_2 coated surface of the final devices shows good levels of cell viability (94%). These data are visually depicted by Fig. 3d.

3.4. Magnetic actuation

The magnetic mobility of silver/titania-coated devices mobility was tested employing the Octomag magnetic manipulation system [54]. Fig. 4a illustrates the working principle of the rolling actuation [60]. The semi-hard magnetic CoNiP layer is premagnetized along a certain direction and presents therefore a remanent magnetization *M*. If a magnetic field *H* is applied to the device, the body aligns so *M* is parallel to *H*. Eq. 4 describes the resulting torque acting on the device where *V* is the volume of magnetic material, *M* is the material magnetization and *B* is the field acting on the device.

$$T = V \vec{M} \times \vec{H} \tag{4}$$

If *H* continuously rotates around a well-defined axis, the final result is a continuous rotation of the device around the same axis. In a way similar to a wheel, this translates into a linear motion when the microrobot is placed on a surface. Direction of the device motion is always perpendicular to the axis around which *H* rotates. If such rotation axis of *H* is varied, the direction of the device can be easily controlled. In the case showed in picture 4b, rotation axis was varied continuously of 360°, resulting in a circular motion of the microrobot. Conversely, the speed of the device can be controlled varying *H* rotation frequency. Hypothetically, if the device perfectly follows the external field, final linear speed is given by Eq. 5, where $2\pi r$ is the circumference of the cylindrical device and τ is the rotation frequency of the magnetic field imposed.

$$v = 2\pi r \, \tau \tag{5}$$

Deviations from this equation are due to friction with the substrate and to the influence of the fluid viscosity in which the device is immersed. Fig. 4d, S9 and S10 clearly show the influence of fluid viscosity

on the performances of the devices (theoretical speed calculated according to Eq. 4 is reported for comparison). When the viscosity of the fluid is relatively low, such in the case of air and water, the samples move at speeds comparable with the theoretical ones at all frequencies. This is a consequence of their relatively large dimension and low speed, which does not determine ultra-low Reynolds numbers. Reynold number is defined by Eq. 6, where ρ is the volumetric mass of the device, *v* is the speed, *d* is the characteristic dimension of the microrobot and μ is the dynamic viscosity of the fluid.

$$Re = \frac{\rho v d}{\mu} \tag{6}$$

If some realistic parameters are considered, resulting Reynolds numbers are detailed in Table 2. Motion in oil (Fig. 4d) happens at considerably low Reynold numbers (indicatively below 1). In such conditions viscous forces start to become predominant over inertial forces [61]. Therefore, fluid viscosity strongly determines the behavior of the device in terms of speed and linearity of the motion. Another effect of a highly viscous environment is the different behavior between devices of different geometry: the PL and the SP samples. At high μ, if geometry is changed, the effect is a different speed at all frequencies. From Fig. 4d, one can see that SP samples move at lower speeds. This effect is a consequence of a totally different fluid dynamic of the device. Fig. 4c visually depicts this effect by moving at constant actuation time two samples, SP and PL, in oil. PL sample moves faster, according to the data presented in Fig. 4d. Geometry can therefore be used to limit or enhance the speed of the device or to control the motion of the fluid around the device itself (for example to better mix the fluid in close proximity of the surface). Interestingly, for frequencies higher than

Table 2
Re numbers calculated for d = 2.5 mm, ρ = 1300 Kg m^{-3} and v = 10 mm s^{-1}.

	Air	Water	Siliconic oil
Dynamic viscosity (Pa s at 20 °C)	1.846×10^{-5}	1.002×10^{-3}	1×10^{-1}
Re number	1760	32.4	0.32

0.9 Hz, the speed of SP microdevices suddenly drops. This phenomenon is similarly observed for helical micro- and nanoswimmers ABFs [62], which exhibit decrease of their translational velocity if the frequency is higher than the step-out frequency for a given rotating magnetic field. When the rotation frequency of *H* field is over the step-out frequency, or in other words, faster than the alignment of *M* with *H*, the device slows down. The step-out frequency was not reached for the PL samples in the range of frequencies employed. This observation highlights the effect of device morphology on the step-out frequency, and also opens the possibility to control differently dissimilar magnetic microrobots. Fig. 4c shows two types of microrobots successfully actuated together on a linear path. Due to their different geometry, the samples can be actuated at different speed in a synchronous way using the same rotating magnetic field. Finally, the possibility to overcome obstacles with the microrobots was investigated. Fig. S11 reports the result of a test performed on a PL sample: the device was actuated linearly over a glass sheet (which was used as step). Increasing thicknesses of the glass sheet were also tested in order to identify the maximum allowed height of the obstacle. It was observed that the devices can overcome a glass step with a thickness that is 50% of the diameter of the microrobot, equal to the radius.

4. Conclusions

Microdevices combining photocatalytic and antibacterial properties were obtained through a smart combination of costless 3D printing and wet metallization techniques. The possibility to apply layers by electrolytic deposition, following a first electroless metallization step to impart conductivity to the surface, was demonstrated by applying different functional films on the devices by mean of a modified barrel plating procedure. Such technique allowed the metallization of many devices at the same time, resulting thus ideal for possible industrial mass production. Obtained coatings were found to be less conformal than their electroless counterparts. Nevertheless, they proved suitable to optimally impart locomotion and water cleaning functionalities to the microdevices. Water cleaning action was investigated for the microdevices produced and the results obtained showed evident photocatalytic and antimicrobial activity. Rhodamine B photodegradation by UV radiation was found to be considerably enhanced by the presence of the microdevices. On the other side, microdevices showed also a good potential for the population control of gram negative bacteria belonging to the *Staphilococcus Aureus* genre. The microrobots obtained in the present work may find application in the water purification inside small water reservoirs and canalizations, possibly with a scaled up magnetic actuation setup. Moreover, the devices can be used for bacteria control also in presence of mammal cells. This fact suggests a possible use also in-vivo inside human body. In conclusion, they are attractive for applications requiring a combination of antimicrobial and photocatalytic functionalities that must be carried out, also separately, in a highly localized and precise way.

Acknowledgements

References

[1] WWDR1, Water for People, Water for Life, (2003) (Accessed 9 September 2017), http://www.unesco.org/new/en/natural-sciences/environment/water/wwap/wwdr/wwdr1-2003/.

[2] A-Z Index of Water-Related Deseases, (2017) (Accessed 9 September 2017), https://www.cdc.gov/healthywater/disease/az.html.

[3] R.L. Jolley, L.W. Condie, J.D. Johnson, S. Katz, R.A. Minear, J.S. Mattice, V.A. Jacobs, Water chlorination: chemistry, environmental impact and health effects, Conf. Water Chlorination Environ. Impact Heal. Eff. 6 (1990).

[4] A. Matilainen, M. Vepsäläinen, M. Sillanpää, Natural organic matter removal by coagulation during drinking water treatment: a review, Adv. Colloid Interface Sci. 159 (2010) 189–197, https://doi.org/10.1016/j.cis.2010.06.007.

[5] E.M. Saggioro, A.S. Oliveira, T. Pavesi, C.G. Maia, L.F.V. Ferreira, J.C. Moreira, Use of titanium dioxide photocatalysis on the remediation of model textile wastewaters containing azo dyes, Molecules 16 (2011) 10370–10386, https://doi.org/10.3390/molecules161210370.

[6] H.G. Kulla, F. Klausener, U. Meyer, B. Lüdeke, T. Leisinger, Interference of aromatic sulfo groups in the microbial degradation of the azo dyes Orange I and Orange II, Arch. Microbiol. 135 (1983) 1–7, https://doi.org/10.1007/BF00419473.

[7] S.K. Sharma, Green Chemistry for Dyes Removal from Waste Water: Research Trends and Applications, John Wiley & Sons, 2015.

[8] M. Kim, E. Steager, J. Agung, Microbiorobotics: Biologically Inspired Microscale Robotic Systems, William Andrew, 2012.

[9] J.J. Abbott, Z. Nagy, F. Beyeler, B. Nelson, Robotics in the small, IEEE Robot. Autom. Mag. 14 (2007) 92–103.

[10] S. Kim, F. Qiu, S. Kim, A. Ghanbari, C. Moon, L. Zhang, B.J. Nelson, H. Choi, Fabrication and characterization of magnetic microrobots for three-dimensional cell culture and targeted transportation, Adv. Mater. 25 (2013) 5863–5868, https://doi.org/10.1002/adma.201301484.

[11] C. Richter, H. Lipson, Untethered hovering flapping flight of a 3D-printed mechanical insect, Artif. Life 17 (2011) 73–86.

[12] K.E. Peyer, S. Tottori, F. Qiu, L. Zhang, B.J. Nelson, Magnetic helical micromachines, Chem. A Eur. J. 19 (2013) 28–38, https://doi.org/10.1002/chem.201203364.

[13] K.E. Peyer, E. Siringil, L. Zhang, B.J. Nelson, Magnetic polymer composite artificial bacterial flagella, Bioinspir. Biomim. 9 (2014) 046014, , https://doi.org/10.1088/1748-3182/9/4/046014.

[14] J. Li, V.V. Singh, S. Sattayasamitsathit, J. Orozco, K. Kaufmann, R. Dong, W. Gao, B. Jurado-Sanchez, Y. Fedorak, J. Wang, Water-driven micromotors for rapid photocatalytic degradation of biological and chemical warfare agents, ACS Nano 8 (2014) 11118–11125.

[15] L. Soler, V. Magdanz, V.M. Fomin, S. Sanchez, O.G. Schmidt, Self-propelled micromotors for cleaning polluted water, ACS Nano 7 (2013) 9611–9620.

[16] E. Karshalev, B. Esteban-Fernández de Ávila, J. Wang, Micromotors for "Chemistry-on-the-Fly, J. Am. Chem. Soc. 140 (2018) 3810–3820.

[17] F. Mushtaq, A. Asani, M. Hoop, X.Z. Chen, D. Ahmed, B.J. Nelson, S. Pané, Highly efficient coaxial TiO2-PtPd tubular nanomachines for photocatalytic water purification with multiple locomotion strategies, Adv. Funct. Mater. 26 (2016) 6995–7002, https://doi.org/10.1002/adfm.201602315.

[18] M. Hoop, Y. Shen, X.Z. Chen, F. Mushtaq, L.M. Iuliano, M.S. Sakar, A. Petruska, M.J. Loessner, B.J. Nelson, S. Pané, Magnetically driven silver-coated nanocoils for efficient bacterial contact killing, Adv. Funct. Mater. 26 (2016) 1063–1069, https://doi.org/10.1002/adfm.201504463.

[19] A. Hong, B. Zeydan, S. Charreyron, O. Ergeneman, S. Pané, M.F. Toy, A.J. Petruska, B.J. Nelson, Real-time holographic tracking and control of microrobots, IEEE Robot. Autom. Lett. 2 (2017) 143–148.

[20] O. Ergeneman, C. Bergeles, M.P. Kummer, J.J. Abbott, B.J. Nelson, Wireless intraocular microrobots: opportunities and challenges, Surg. Robot. Springer (2011) 271–311.

[21] K.M. Sivaraman, G. Chatzipirpiridis, B. Becsek, T. Lühmann, O. Ergeneman, B.J. Nelson, S. Pané, Functional polypyrrole coatings for wirelessly controlled magnetic microrobots, IEEE EMBS Spec. Top. Conf. Point-of-Care Healthc. Technol. Synerg. Towar. Better Glob. Heal. PHT 2013 (2013) 22–25, https://doi.org/10.1109/PHT.2013.6461275.

[22] R. Bernasconi, F. Cuneo, E. Carrara, G. Chatzipirpiridis, M. Hoop, X. Chen, B.J. Nelson, R. Pané, C. Credi, M. Levi, L. Magagnin, Hard-magnetic cell microscaffolds from electroless coated 3D printed architectures, Mater. Horizons 5 (2018) 699–707, https://doi.org/10.1039/C8MH00206A.

[23] I. Gibson, D.W.D.W. Rosen, B. Stucker, Additive Manufacturing Technologies: Rapid Prototyping to Direct Digital Manufacturing, Springer, 2009, https://doi.org/10.1007/978-1-4419-1120-9.

[24] R. Bernasconi, C. Credi, M. Tironi, M. Levi, L. Magagnin, Electroless metallization of stereolithographic photocurable resins for 3D printing of functional microdevices, J. Electrochem. Soc. 164 (2017) B3059–B3066, https://doi.org/10.1149/2.0081705jes.

[25] A. Wild, Integration of functional circuits into FDM parts, Adv. Mater. Res. Trans. Tech. Publ. (2014) 29–33.

[26] K. Angel, H.H. Tsang, S.S. Bedair, G.L. Smith, N. Lazarus, Selective electroplating of 3D printed parts, Addit. Manuf. 20 (2018) 164–172.

[27] A. Bertsch, P. Renaud, Microstereolithography, Three-dimensional Microfabr. Using Two-Phot. Polym. Elsevier, 2016, pp. 20–44.

[28] G.W. Bishop, 3D printed microfluidic devices, Microfluid. Biol. Fundam. Appl. 8 (2016) 103–113, https://doi.org/10.1007/978-3-319-40036-5_4.

[29] E. Aguilera, J. Ramos, D. Espalin, F. Cedillos, D. Muse, R. Wicker, E. MacDonald, 3D printing of electro mechanical systems, Proc. Solid Free. Fabr. Symp. (2013) 950–961.

[30] K. Willis, E. Brockmeyer, S. Hudson, I. Poupyrev, Printed optics: 3D printing of embedded optical elements for interactive devices, Proc. 25th Annu. ACM Symp. User Interface Softw. Technol. (2012) 589–598.

[31] A. Joe Lopes, E. MacDonald, R.B. Wicker, Integrating stereolithography and direct

print technologies for 3D structural electronics fabrication, Rapid Prototyp. J. 18 (2012) 129–143.

[32] F. Inoue, Y. Harada, M. Koyanagi, T. Fukushima, K. Yamamoto, S. Tanaka, Z. Wang, S. Shingubara, Perfect conformal deposition of electroless Cu for high aspect ratio through-Si vias, Electrochem. Solid-State Lett. 12 (2009) H381, https://doi.org/10.1149/1.3193535.

[33] D.Y. Park, N.V. Myung, M. Schwartz, K. Nobe, Nanostructured magnetic CoNiP electrodeposits: structure-property relationships, Electrochim. Acta 47 (2002) 2893–2900, https://doi.org/10.1016/S0013-4686(02)00160-3.

[34] J.L. Clement, P.S. Jarrett, Antibacterial silver, Met. Drugs 1 (1994) 467–482, https://doi.org/10.1155/MBD.1994.467.

[35] S.L. Percival, P.G. Bowler, D. Russell, Bacterial resistance to silver in wound care, J. Hosp. Infect. 60 (2005) 1–7, https://doi.org/10.1016/j.jhin.2004.11.014.

[36] Q.L. Feng, J. Wu, G.Q. Chen, F.Z. Cui, T.N. Kim, K.J. O, A mechanistic study of the antibacterial effect of silver ions on Escherichia coli and Staphylococcus aureus, J. Biomed. Mater. Res. 52 (2000) 662–668, https://doi.org/10.1002/1097-4636(20001215)52:43.0.CO;2-3.

[37] A. Panáček, L. Kvitek, R. Prucek, M. Kolávr, R. Večevrová, N. Pizúrová, V.K. Sharma, T. Nevěčná, R. Zbovril, Silver colloid nanoparticles: synthesis, characterization, and their antibacterial activity, J. Phys. Chem. B 110 (2006) 16248–16253.

[38] J.R. Morones-Ramirez, J.A. Winkler, C.S. Spina, J.J. Collins, Silver enhances antibiotic activity against gram-negative bacteria, Sci. Transl. Med. 5 (2013), https://doi.org/10.1126/scitranslmed.3006276 190ra81-190ra81.

[39] A. Lansdown, Siver in healthcare: antimicrobial effects and safety in use, Biofunctional Text. Ski. 33 (2006) 17–34.

[40] U.I. Gaya, A.H. Abdullah, Heterogeneous photocatalytic degradation of organic contaminants over titanium dioxide: a review of fundamentals, progress and problems, J. Photochem. Photobiol. C Photochem. Rev. 9 (2008) 1–12.

[41] L. Lin, W. Lin, Y. Zhu, B. Zhao, Y. Xie, Phosphor-doped titania —a novel photocatalyst active in visible light, Chem. Lett. 34 (2005) 284–285, https://doi.org/10.1246/cl.2005.284.

[42] K. Wilke, H.D. Breuer, The influence of transition metal doping on the physical and photocatalytic properties of titania, J. Photochem. Photobiol. A: Chem. 121 (1999) 49–53, https://doi.org/10.1016/S1010-6030(98)00452-3.

[43] H. Kisch, S. Sakthivel, M. Janczarek, D. Mitoraj, A low-band gap, nitrogen-modified titania visible-light photocatalyst, J. Phys. Chem. C 111 (2007) 11445–11449, https://doi.org/10.1021/jp066457y.

[44] S. Malato, P. Fernández-Ibáñez, M.I. Maldonado, J. Blanco, W. Gernjak, Decontamination and disinfection of water by solar photocatalysis: recent overview and trends, Catal. Today 147 (2009) 1–59, https://doi.org/10.1016/j.cattod.2009.06.018.

[45] B. Ohtani, K. Iwai, H. Kominami, T. Matsuura, Y. Kera, S. ichi Nishimoto, Titanium (IV) oxide photocatalyst of ultra-high activity for selective N-cyclization of an amino acid in aqueous suspensions, Chem. Phys. Lett. 242 (1995) 315–319, https://doi.org/10.1016/0009-2614(95)00740-U.

[46] L.A. Brook, P. Evans, H.A. Foster, M.E. Pemble, A. Steele, D.W. Sheel, H.M. Yates, Highly bioactive silver and silver/titania composite films grown by chemical vapour deposition, J. Photochem. Photobiol. A: Chem. 187 (2007) 53–63, https://doi.org/10.1016/j.jphotochem.2006.09.014.

[47] D.W. Sheel, L.A. Brook, I.B. Ditta, P. Evans, H.A. Foster, A. Steele, H.M. Yates, D.W. Sheel, L.A. Brook, I.B. Ditta, P. Evans, H.A. Foster, A. Steele, H.M. Yates,

[48] F.C. Walsh, C. Ponce de Leon, A review of the electrodeposition of metal matrix composite coatings by inclusion of particles in a metal layer: an established and diversifying technology, Trans. IMF 92 (2014) 83–98, https://doi.org/10.1179/0020296713Z.000000000161.

[49] V.S. Protsenko, E.A. Vasil'Eva, A.V. Tsurkan, A.A. Kityk, S.A. Korniy, F.I. Danilov, Fe/TiO2 composite coatings modified by ceria layer: electrochemical synthesis using environmentally friendly methanesulfonate electrolytes and application as photocatalysts for organic dyes degradation, J. Environ. Chem. Eng. 5 (2017) 135–146, https://doi.org/10.1016/j.jece.2016.11.034.

[50] E.S. Chen, G.R. Lakshminarayanan, F.K. Sautter, The codeposition of alumina and titania with copper, Metall. Trans. 2 (1971) 937–942, https://doi.org/10.1007/BF02664222.

[51] A. Méndez-Albores, S.G. González-Arellano, Y. Reyes-Vidal, J. Torres, Ş. Ţălu, B. Cercado, G. Trejo, Electrodeposited chrome/silver nanoparticle (Cr/AgNPs) composite coatings: characterization and antibacterial activity, J. Alloys. Compd. 710 (2017) 302–311, https://doi.org/10.1016/j.jallcom.2017.03.226.

[52] N. Board, The Complete Technology Book on Electroplating, Phosphating, Powder Coating And Metal Finishing, ASIA PACIFIC BUSINESS PRESS Inc., 2005.

[53] L. Wang, L. Sun, J. Li, Electroless copper plating on Fraxinus mandshurica veneer using glyoxylic acid as reducing agent, Bioresources 6 (2011) 3493–3504.

[54] M.P. Kummer, J.J. Abbott, B.E. Kratochvil, R. Borer, A. Sengul, B.J. Nelson, Octomag: an electromagnetic system for 5-DOF wireless micromanipulation, IEEE Trans. Robot. 26 (2010) 1006–1017, https://doi.org/10.1109/TRO.2010.2073030.

[55] A. Mills, C. Hill, P.K.J. Robertson, Overview of the current ISO tests for photocatalytic materials, J. Photochem. Photobiol. A: Chem. 237 (2012) 7–23, https://doi.org/10.1016/j.jphotochem.2012.02.024.

[56] S. Spanou, A.I. Kontos, A. Siokou, A.G. Kontos, N. Vaenas, P. Falaras, E.A. Pavlatou, Self cleaning behaviour of Ni/nano-TiO2 metal matrix composites, Electrochim. Acta 105 (2013) 324–332, https://doi.org/10.1016/j.electacta.2013.04.174.

[57] L. Magagnin, R. Bernasconi, S. Ieffa, M.V. Diamanti, D. Pezzoli, G. Candiani, M.P. Pedeferri, Photocatalytic and antimicrobial coatings by electrodeposition of silver/TiO2 nano-composites, ECS Trans. 45 (2013) 1–6.

[58] N.G. Asenjo, R. Santamaría, C. Blanco, M. Granda, P. Álvarez, R. Menéndez, Correct use of the Langmuir-Hinshelwood equation for proving the absence of a synergy effect in the photocatalytic degradation of phenol on a suspended mixture of titania and activated carbon, Carbon N. Y. 55 (2013) 62–69, https://doi.org/10.1016/j.carbon.2012.12.010.

[59] M. Skladanowski, P. Golinska, K. Rudnicka, H. Dahm, M. Rai, Evaluation of cytotoxicity, immune compatibility and antibacterial activity of biogenic silver nanoparticles, Med. Microbiol. Immunol. 205 (2016) 603–613, https://doi.org/10.1007/s00430-016-0477-7.

[60] G. Chatzipirpiridis, E. Avilla, O. Ergeneman, B.J. Nelson, S. Pane, Electroforming of magnetic microtubes for microrobotic applications, IEEE Trans. Magn. 50 (2014) 10–12, https://doi.org/10.1109/TMAG.2014.2325671.

[61] E.M. Purcell, Life at low Reynolds number, Am. J. Phys. 45 (1977) 3–11, https://doi.org/10.1119/1.10903.

[62] L. Zhang, J.J. Abbott, L. Dong, K.E. Peyer, B.E. Kratochvil, H. Zhang, C. Bergeles, B.J. Nelson, Characterizing the swimming properties of artificial bacterial flagella, Nano Lett. 9 (2009) 3663–3667, https://doi.org/10.1021/nl901869j.